Article

Multinary alloying for facilitated cation exchange and suppressed defect formation in kesterite solar cells with above 14% certified efficiency

Jiangjian Shi [1,6], Jinlin Wang[1,2,6], Fanqi Meng [3,6], Jiazheng Zhou[1,2,6], Xiao Xu[1,2], Kang Yin[1,2], Licheng Lou[1,2], Menghan Jiao[1,2], Bowen Zhang[1,2], Huijue Wu[1], Yanhong Luo [1,2,4], Dongmei Li [1,2,4] & Qingbo Meng [1,2,4,5] ✉

Kesterite $Cu_2ZnSn(S, Se)_4$ (CZTSSe) solar cells are highly promising low-cost thin-film photovoltaics. However, the efficiency of these solar cells is challenged by severe charge losses and complex defects. Here we reveal through a data-driven correlation analysis that the dominant deep defect in CZTSSe exhibits a donor character. We further propose that incomplete cation exchange in the multi-step crystallization reactions of CZTSSe is the kinetic mechanism responsible for the defect formation. To facilitate the cation exchange, we introduce a multi-elemental alloying approach aimed at weakening the metal–chalcogen bond strength and the stability of intermediate phases. This strategy leads to a significant reduction in charge losses within the CZTSSe absorber and to a total-area cell efficiency of 14.6% (certified at 14.2%). Overall, these results not only present a significant advancement for kesterite solar cells but could also help identify and regulate defects in photovoltaic materials.

The ongoing exploration of diversified photovoltaic materials has created more opportunities for the efficient, low-cost and environmentally friendly utilization of solar energy[1,2]. The emerging multinary chalcogenide, $Cu_2ZnSn(S, Se)_4$ (CZTSSe), is being developed as a promising candidate to promote the large-scale and low-cost application of thin-film photovoltaics by taking advantage of its high constituent element abundance, non-toxicity and excellent industrial compatibility[3–7]. However, multinary element components in CZTSSe have also led to complex atomic self-doping and intrinsic defects, resulting in severe non-radiative charge recombination and significant photoelectric conversion efficiency (PCE) loss in solar cells[2,8,9].

In the past years, several types of defect such as Cu/Zn disorder, Sn vacancies (V_{Sn}) and Sn/Zn substitutions (Sn_{Zn}), located on the CZTSSe surface, CZTSSe/CdS interface or grain boundaries, have been successively considered as dominant pathways in causing charge loss in the cells[2,5,7–10]. On the basis of these understandings, a variety of approaches have been employed aiming at increasing the thermodynamic formation energy of defects to reduce their concentration, such as a fine optimization of Sn element content, introducing Ag/Cu substitution doping and modification of Fermi energy level by carrier doping[10–13]. These efforts have resulted in CZTSSe solar cells achieving baseline efficiencies of over 12% in more and more research groups[7,14–18]. Recently, a record PCE of 13.0% was achieved through

heterojunction annealing-induced interface reconstruction[5], and a PCE of 13.8% was also reported by us using high-pressure-assisted regulation of phase evolutions[19]. However, further regulating defects to achieve higher PCE in CZTSSe solar cells remains highly challenging, especially because the microscopic charge loss pathway in the cell, and the specific defect responsible for the efficiency loss has not been definitively identified in experiments[2,7,20,21]. Moreover, the widely used thermodynamic equilibrium mechanism may not have fully reflected the defect formation in CZTSSe because its crystallization is primarily governed by kinetics-related solid-state heterogeneous reactions[16,22,23]. Kinetic processes are typically more complex than that predicted by end-state equilibrium theories, which renders the widely explored thermodynamic regulation route less effective in suppressing defects further in the cell. Therefore, more precisely identifying the defect, more comprehensively understanding the defect formation mechanism and more effectively regulating their formation processes are currently the most critical requirement for CZTSSe solar cells.

Here we present a kinetics-based approach to suppress the formation of deep defects in CZTSSe, resulting in a remarkable improvement of the cell PCE up to 14.6%. By proposing a cell performance parameter analysis method, we identify the donor-type defect, most possibly the Sn_{Zn}, as the primary deep defect in CZTSSe. We further suggest that the incomplete cation exchange in the multi-step crystallization reactions of CZTSSe is the primary kinetic mechanism responsible for the formation of this defect. These findings lead us to introduce elemental alloying to reduce the material stability and metal–chalcogen bond strength of the intermediate phases, thereby facilitating the cation exchange. This approach has significantly reduced the deep defect-induced charge loss in the CZTSSe absorber and consequently resulted in an impressive step forward in the cell PCE. In addition, the presented defect analysis method and the understanding of the defect formation mechanism in this work also have implications for the defect regulation in other photovoltaic materials.

Defect identification of CZTSSe

To overcome the inconsistency of defect measurement met in previous works[21], here we propose using the correlations between cell performance parameters with defect characteristics to evaluate the type of killer defect in CZTSSe. Using device simulation (Supplementary Table 1)[24,25], we found that currently the voltage and PCE loss in the cells is dominated by deep defect-related non-radiative recombination in bulk CZTSSe absorbers (Supplementary Figs. 1–4). We further observed that the cells governed by different types of deep defect (acceptor or donor) exhibit distinct J_{SC}, V_{OC} and FF evolution behaviours when the cell PCE gradually decreases as the cell defect concentration and carrier-capture cross section (σ) increase (Supplementary Fig. 3; J_{SC}, short-circuit current density; V_{OC}, open-circuit voltage; FF, fill factor). Specifically, under the same PCE, the cells with donor defects exhibit higher J_{SC} but lower V_{OC} and FF due to the charge compensation between donor defects and majority holes in the CZTSSe absorber. This discrepancy is more clearly observed by introducing a combined parameter, $J_{SC}/(V_{OC} \times FF)$, and it can be seen in Fig. 1a that the cells with different defect type segregate into two regions in the $J_{SC}/(V_{OC} \times FF)$-PCE characteristics graph. These behaviours make the $J_{SC}/(V_{OC} \times FF)$-PCE characteristics a reliable criterion for identifying the deep defect type.

We subsequently collected performance parameters on approximately 1,000 cells from our laboratory and compared them with the simulation results[26,27]. We assume that the fluctuation in the PCE of these cells is mainly caused by variations in the concentration or σ of deep defects in CZTSSe, as the formation of defects is the most uncontrollable variable in experiment. Figure 1b shows that nearly all the experimental data fall within the donor defect region, indicating that the cell's PCE is mainly determined by deep donor defect. This finding differs from previously proposed scenarios of acceptor-type

deep defects[10,28] but is supported by recent theoretical predictions[9]. Additionally, the similar distribution trend of the $J_{SC}/(V_{OC} \times FF)$-PCE data between different cell groups suggests that these CZTSSe absorbers have the same defect character despite that they were fabricated by different experimenters and with different methods. As in Fig. 1b, by comparing the experimental trend with the simulation results derived from fixed σ parameters (dashed lines), we estimated these CZTSSe absorbers having the σ in the order of 10^{-14} cm^2. We also measured the photoluminescence (PL) quenching activation energy (E_a^{PL}) of the CZTSSe films, which gave values in the range between 50 and 70 meV (Fig. 1c). These small E_a^{PL} values agree with the large σ and are very close to the predicted carrier-capture energy barrier of Sn_{Zn} donor defect[8,9,29,30]. Therefore, we determine that the primary deep defect in these cells is Sn_{Zn}.

Kinetic mechanism for the defect formation

It was previously predicted that the cell PCE limited by Sn_{Zn} defect can reach 20% or higher[8,9,30], which is significantly better than currently achieved experimental results. This implies that the defect formation process in current CZTSSe absorbers is deviated from the thermodynamic equilibrium and that the defect concentration is obviously higher than the predicted ones. In our opinion, incomplete cation exchange within the CZTSSe multi-step solid-phase crystallization reactions is a more important factor influencing the formation of Sn_{Zn} defect. In the initial crystallization stage, in addition to the direct formation of CZTSSe phase within the film, ternary $Cu_2Sn(S, Se)_3$ (CTSSe) and binary $Zn(S, Se)$ intermediate phases can simultaneously emerge, due to their lower requirements for selenization temperature and Se concentration (Supplementary Fig. 5)[31–34]. To make these intermediate phases transform into final CZTSSe, Zn needs to release from $Zn(S, Se)$ and partially exchange with Cu and Sn in CTSSe, as schematically shown in Fig. 2a,b. Although this reaction is thermodynamically favourable at high temperatures, the energy barriers of metal–Se bond breaking and atom insertion in these processes still limit the kinetics of Zn/Sn and Zn/Cu exchanges, thus leading to the formation of Sn_{Zn} defect in the final CZTSSe. As such, to reduce this defect, cation exchange needs to be facilitated by decreasing the intermediate-phase stability and reducing the cation-exchange barrier, as shown by the dashed line in Fig. 2b.

Elemental alloying strategy

To achieve this goal, elemental alloying offers a promising solution as it can effectively modify the atomic bonding state of a material[35,36]. Initially, we used material formation energy (E_{form}) as a criterion to search suitable alloying elements. To avoid introducing carrier doping, only +1, +2 and +4 valent elements were considered. We collected and compared the E_{form} of a variety of A_2BSe_3 (A: Na, K, Ag, Cu; B: Si, Ge) and MSe (M: Ca, Mg, Cd) compounds with that of Cu_2SnSe_3 and ZnSe (Supplementary Table 2)[37,38]. Figure 2c shows that Ag- or Ge-containing A_2BSe_3 compounds have a smaller $|E_{form}|$, making them potential alloying elements. CdSe in MSe also exhibits a similar trend. We further calculated the Gibbs free energy of CTSe, ZnSe and their alloyed compounds with these three elements. As shown in Fig. 2d, Ag alloying in CTSe increases the free energy by approximately 0.9 eV at 800 K, and Cd alloying in ZnSe increases the free energy by about 2.0 eV at 800 K. Ge has little influence on the free energy. We further calculated the change in the metal–Se bond energy of these compounds caused by the alloying (Supplementary Figs. 6–8). The results shown in Fig. 2e indicate that the average energy of the metal–Se bond around the alloying site is reduced by approximately 0.16 (Ag–Cu), 0.04 (Ge–Sn) and 0.11 eV (Cd–Zn), respectively. For ZnSe, the reduced 0.11 eV has reached one-fourth of its initial bond energy[39]. These results mean that in the high-temperature reaction process, these alloyed intermediate phases become less stable, and thus the cation exchange involving metal–Se bond breaking and reconstruction will be much easier, which will facilitate the elimination of Sn_{Zn} defect in the final CZTSSe.
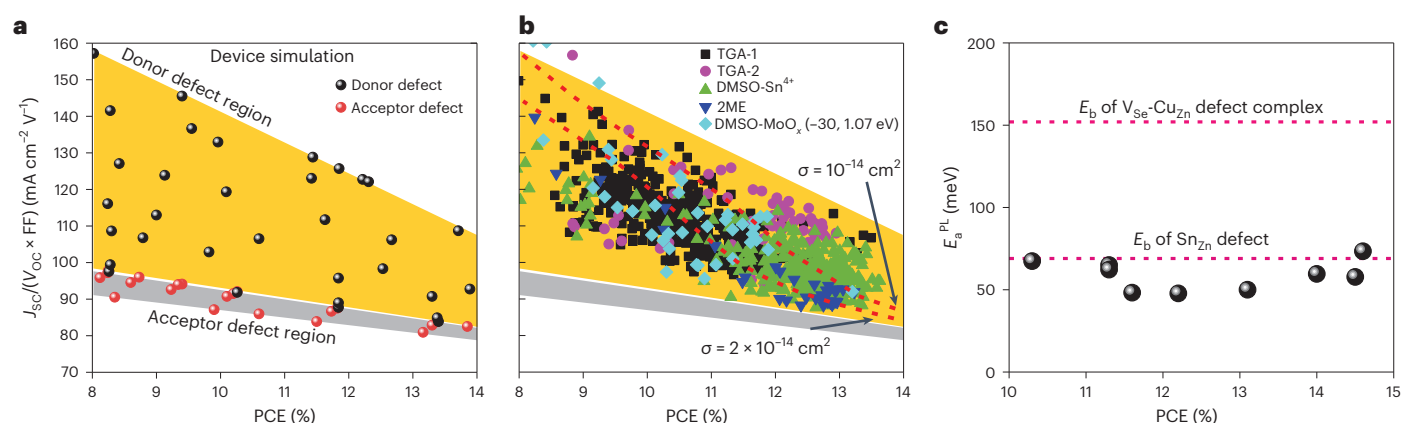
Fig. 1 | Defect-type analysis of CZTSSe. a, Impact of defect type (donor and acceptor) on the $J_{SC}/(V_{OC} \times FF)$-PCE characteristics of kesterite solar cells. The solid points are simulation results of the cells with different defect characters (concentration and σ); the shadows depict the regions dominated by donor or acceptor defect. **b**, A comparison of experimental data to the simulation results. The experimental data were collected from ~1,000 cells fabricated by different experimenters and with different methods in our lab (TGA-1 (or 2), thioglycolic acid–water solution method and experimenter 1 (or 2); DMSO-Sn⁴⁺, dimethyl

sulfoxide solution method with SnCl$_4$ as the Sn source; 2ME, 2-methoxyethanol solution method; DMSO-MoO$_x$, back-interface modification by MoO$_x$, and the bandgap of the CZTSSe is about 1.07 eV). The dashed lines are simulation results corresponding to σ of 10^{-14} and 2×10^{-14} cm², respectively. **c**, PL quenching activation energy (E_a^{PL}) of CZTSSe films corresponding to the cells with different PCEs. Dashed lines depict the calculated carrier-capture energy barrier (E_b) of several defects (or defect complexes) for reference.

Characterization of alloyed CZTSSe films

In experimental studies, the aforementioned alloying elements Ag and Cd were directly introduced via the precursor solution, and the Ge was introduced from the back interface. The precursor solutions were subsequently deposited onto soda lime glass/Mo substrates by cycled coating, and final CZTSSe absorber films were obtained through selenization. To study the influence of the alloying, we first characterized the unalloyed (control) and optimally alloyed (target) films at different crystallization stages. The samples were obtained by interrupting the selenization process (Supplementary Figs. 9 and 10), and they are labelled according to the interrupting time–temperature point for clarity here. For example, 9–502 means the film selenization had experienced 9 min and was interrupted at 502 °C. The films were first characterized using a spherical aberration corrected scanning transmission electron microscope (STEM). Cross-sectional high-angle annular dark-field (HAADF) images (Fig. 3a and Supplementary Fig. 11) reveal that the target and control samples adopt a similar top-down crystallization mode and have the same crystal growth orientation along the [201] direction of the kesterite lattice (Supplementary Figs. 11 and 12). The top region of the films has transformed into large grains, whereas the lower region remains in a mixed nanocrystal-amorphous state or amorphous state (Supplementary Fig. 13). In the lower region of the target 9–502 sample, a simultaneous enrichment of Zn and Cd in some nanoscale domains can be observed from the energy dispersive X-ray spectroscopy (EDX) mapping image (Fig. 3b). Electron energy loss spectroscopy also reveals the coexistence of Ag/Cu or Cd/Zn in different nanocrystals within the mixed layer (Fig. 3c). Furthermore, in top CZTSSe grains, an occupation of Ag at Cu site and an existence of Ge are also confirmed (Supplementary Figs. 14 and 15). These findings indicate that elemental alloying did occur in the initial crystallization reaction stage.

We further conducted a detailed analysis of the element distribution within the interface region of the top grain/mixed nanocrystal-amorphous layers in 9–502 and 11–540 samples (Supplementary Fig. 16). As illustrated by the dashed lines in Fig. 3d, both Zn and Sn demonstrate a gradient in element distribution within this region. According to Fick's first law, this gradient reflects the upward diffusion of elements, combining into the top grains. It can be further seen that the alloying in the target samples has increased the Zn element gradient compared with that in the control samples and moreover

rendered it similar to that of Sn. This observation suggests an enhancement in the activity of Zn element insertion into the top crystals. Consequently, Zn acquired a more synchronized distribution with Cu and Sn elements throughout the film (Fig. 3e,f and Supplementary Figs. 17 and 18). In comparison, in the control sample, Zn exhibited low reaction activity with Cu and Sn and thus has been repelled to the middle region.

The evolution of X-ray diffraction (XRD) patterns was also studied. As seen in Fig. 3g, in the target sample, the final-like CZTSSe phase with an XRD peak at about 27.2° already appeared at the 8–464 selenization point, whereas in the control sample, this phase did not appear until two minutes later (10–540). Moreover, the XRD peak position of this phase in the target sample remained constant throughout the selenization process, which is significantly different from the evolution phenomenon of the control sample (Supplementary Figs. 19 and 20). Additionally, the Raman spectra of the target sample shown in Fig. 3h display a more pronounced Zn-related lattice vibration (150–175 cm⁻¹) and a much weaker CTSSe signature (180 cm⁻¹)[30]. The X-ray photoelectron valence-band spectra also demonstrate an enhancement of Zn–Se(S) hybridization in CZTSSe (Supplementary Fig. 21)[40,41]. These results further confirm that elemental alloying has facilitated the exchange of Zn/Sn and Zn/Cu, leading to an accelerated formation of ordered kesterite phase. This, in turn, is expected to help suppress the formation of Sn$_{Zn}$ deep defect.

Solar cell characterization

We subsequently fabricated CZTSSe solar cells and analysed their performance. The statistics of a batch of cells are presented in Fig. 4a and Supplementary Fig. 22. The $J_{SC}/(V_{OC} \times FF)$-PCE analysis revealed that all cells followed the donor defect characteristics. The target cell had an average PCE of about 13.5%, whereas the control cell had an average PCE of only about 10.5%. The PCE improvement was mainly attributed to the increase in V_{OC} and FF, due to reduced charge recombination loss. We also fabricated cells with more alloying groups, as shown in Supplementary Fig. 23. The best result was obtained when Ag, Ge and Cd were synergistically used (Supplementary Fig. 24), where Ag/Ge modified CTSSe and Cd modified Zn(S, Se) phase, respectively, in the crystallization process. We also attempted to use Ag/Ge/Mg to alloy the CZTSSe but obtained obviously lower PCE (Supplementary Fig. 25). Thus, using the E_{form} to theoretically search alloying elements is feasible. Furthermore, we attempted a post-deposition treatment method to
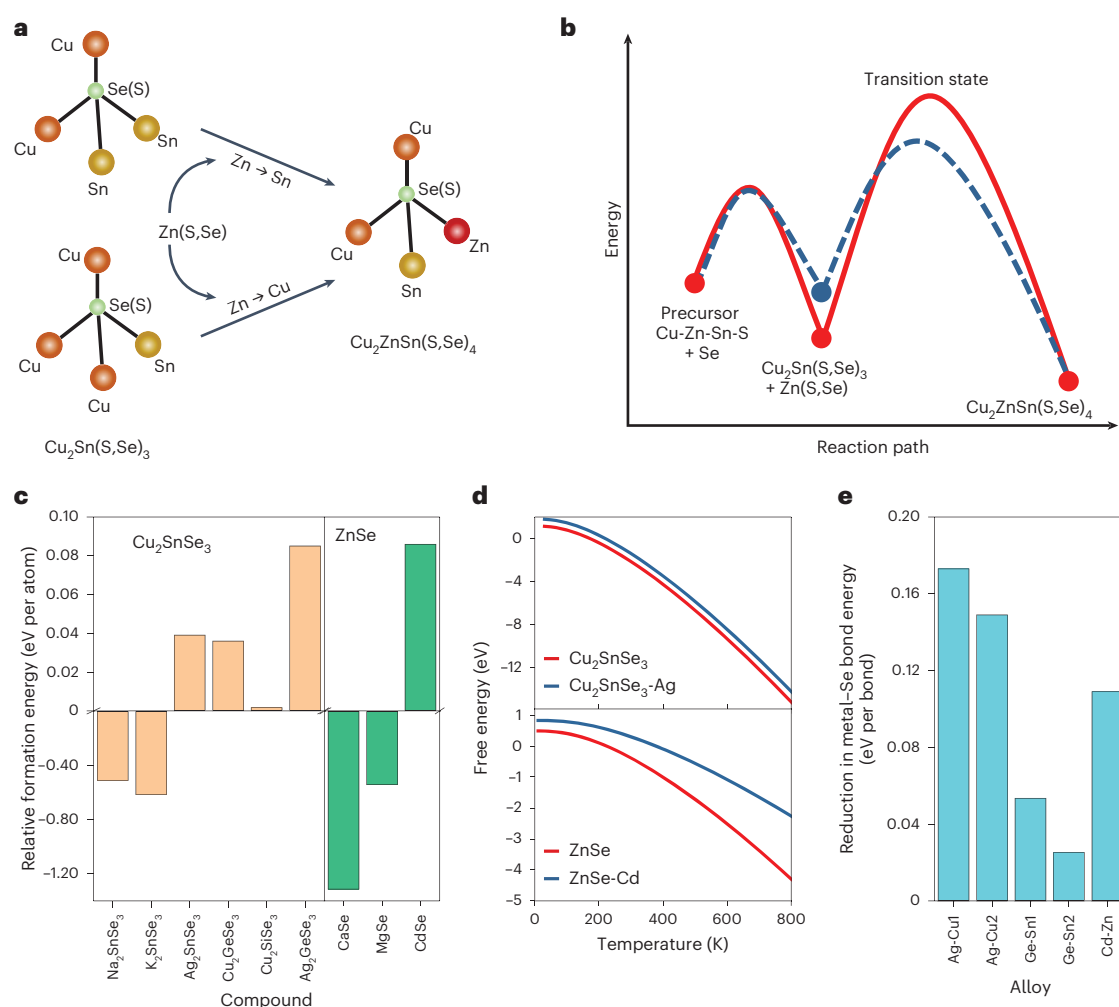
Fig. 2 | Kinetic mechanism and regulation of Sn$_{Zn}$ defect formation. a,b, Schematic diagrams of cation-exchange processes in the phase evolution from CTSSe to CZTSSe (**a**) and of the multi-step reaction pathways (**b**). The primitive Se–metal coordination structures in CTSSe and CZTSSe are given here to show their evolutions. **c**, Relative formation energy of A_2BSe$_3$ (A: Na, K, Ag, Cu; B: Si, Ge) and MSe (M: Ca, Mg, Cd) compounds compared with Cu$_2$SnSe$_3$ and ZnSe, respectively. **d**, Gibbs free energy of Cu$_2$SnSe$_3$, ZnSe and their alloyed compounds. **e**, Reduction in the metal–Se bond energy of Cu$_2$SnSe$_3$ and ZnSe when they are partially alloyed. The lattice configurations used for these calculations are shown in Supplementary Figs. 6–8.

introduce these alloying elements, but it did not work well. This implies that compared with final-state doping, it is more important for these elements to participate in and regulate the crystallization reactions.

Thermal admittance spectroscopy was used to characterize the defect[42]; however, only shallow defects with ionization energy of about 0.09 eV were measured in both cells (Supplementary Fig. 26). We turned to quantify the deep defect-induced charge recombination loss in the cell using a modulated electrical transient method (Supplementary Note 1 and Supplementary Figs. 27 and 28)[43,44]. The photovoltage decay rate (k_r) of the cells was extracted from the modulated transient photovoltages, as shown in Fig. 4b, which exhibits exponential increases with the voltage. On the basis of this characteristic, the ideality factor (A) of the control and target cells was fitted to be 1.93 and 1.55, respectively. The significant reduction in the ideality factor indicates that the charge recombination in the CZTSSe absorber has been effectively suppressed. The charge extraction (η_E) and collection efficiencies (η_C) correlated with the charge loss in the CZTSSe and buffer/window layer, respectively, were further extracted from the measurements. As shown in Fig. 4c, the η_C of these two cells is comparable to each other in the entire voltage regime. In contrast, η_E of the target cell has been significantly enhanced and is even higher than the η_C in the high-voltage regime. This suggests that the charge non-radiative recombination loss

in the CZTSSe film has indeed been reduced. Considering the similar valence-band edge and lattice vibration properties between these two samples (Supplementary Figs. 29 and 30), the improvement in η_E is attributed to an obvious reduction in the defect concentration (Supplementary Fig. 31).

We conducted further PL characterization of the CZTSSe films, which emit photons below the bandgap (E_g) at low temperatures. Our analysis revealed that the PL red shift (relative to the E_g) of the target film is reduced by about 20 meV compared with the control sample (Fig. 4d). This suggests a decrease in the potential fluctuation induced by deep defects[10,45]. To evaluate the surface electric properties, we measured the contacting potential difference (CPD) of these samples[46]. As shown in Fig. 4e, both films exhibited similar energy band upward bending behaviour in the grain boundary regions, and their CPD properties were not significantly affected by light illumination (Supplementary Fig. 32). This implies that both films have negligible surface and grain boundary carrier pinning effect[47]. Consequently, all these results demonstrate that the benefit of the elemental alloying lies in reducing deep defects in CZTSSe grain interiors.

The current–voltage characteristics of our champion cell are presented in Fig. 4f, showing a total-area PCE of 14.6% (active-area PCE: ~15.1%). The cell achieved a J_{SC} of 36.6 mA cm^{-2}, a V_{OC} of 0.55 V

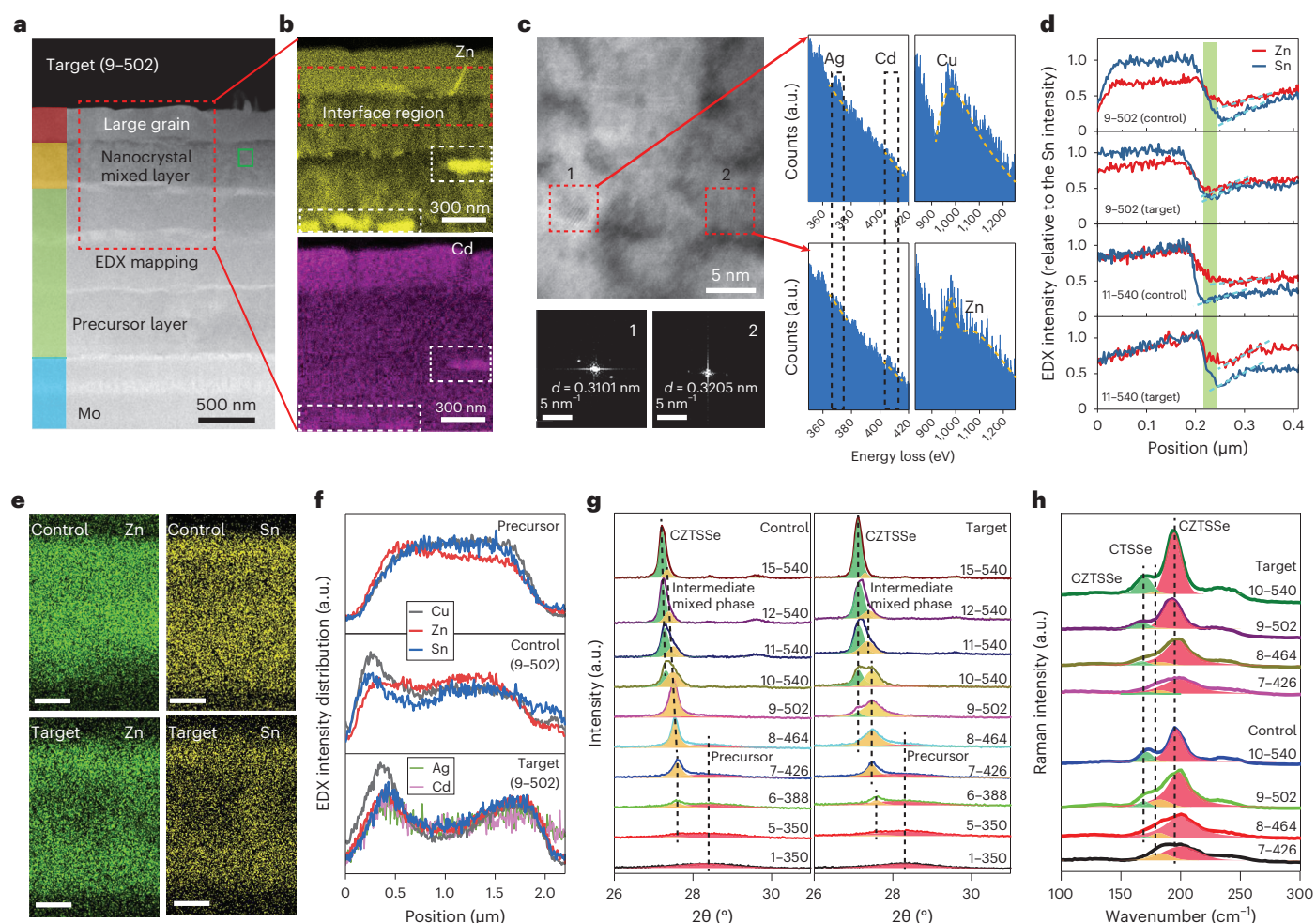**Fig. 3 | Influence of elemental alloying on the solid-phase reaction in CZTSSe films. a**, Cross-sectional HAADF STEM image of the target 9–502 film. **b**, STEM EDX (Zn and Cd) images of a selected region in the target film. The nanoscale regions with simultaneous enrichment of Zn and Cd are marked up with white dashed boxes. **c**, HAADF image of a selected region in the nanocrystal mixed layer, and fast Fourier transform patterns and electron energy loss spectra of two observed nanocrystals. *d* is the derived interplanar spacing. The dashed lines are guidance for the eyes. **d**, Zn and Sn element distribution crossing the top grain/mixed layer interface. The studied region is schematically shown by a red dashed box in Fig. 3b. The gradient of element intensity is depicted by dashed blue lines. **e**,**f**, Cross section SEM EDX mapping image (**e**) and element distribution profiles of the 9–502 films (**f**). Scale bars, 500 nm. **g**,**h**, Evolutions of X-ray diffraction patterns (**g**) and Raman spectra (**h**) of the films in the selenization process. The shadows reflect different phases derived from multi-peak fittings using Voigt function. In the multi-peak fittings, the number, centre and broadening of the peaks have been iteratively optimized to realize the smallest residuals. The dashed lines are guidance for the eyes.

and an FF of 0.724. Furthermore, the cell obtained a certified PCE of 14.2% in an accredited independent laboratory (National PV Industry Measurement and Testing Center; Supplementary Fig. 33). The main discrepancy between the certified and our lab result, that is, the FF, is attributed to the influence of the MgF$_2$ antireflection layer on the electrical probe contacting. The cell's external quantum efficiency (EQE) spectrum (Fig. 4g) yielded an integrated J_{SC} of 38.0 mA cm^{-2} and an E_g of 1.08 eV. Additional performance parameters of our cell and previously reported cells are summarized in Table 1 (refs. 5,14,15,19). The ratio of our J_{SC} to the Shockley–Queisser limit (J_{SC}/J_{SC}^{SQ}) is approximately 0.82, similar to the 12.6% record cells. Moreover, the V_{OC}FF/V_{OC}^{SQ}FF^{SQ} value of our cell reaches 0.55, and the V_{OC} deficit ($E_g/q - V_{OC}$) has been reduced to 0.530 V. These two parameters outperform those obtained in our previous cells fabricated using high reaction chamber pressure[19]. These results indicate that multinary alloying can more effectively regulate the reaction kinetics to suppress deep defects in CZTSSe and thus creates more favourable moderate reaction conditions to meet the requirements of large-scale and low-cost industrial manufacturing. Overall, these results represent a significant advancement for CZTSSe

solar cells, which could also further promote the development of emerging inorganic thin-film solar cells (Fig. 4h)[48].

Multinary alloying has become a baseline strategy in our experiment due to its significant and reproducible effect in improving the performance of kesterite solar cells. Nonetheless, regarding the mechanism of alloying in regulating the CZTSSe crystallization, several open questions still need to be further studied. First, we need to further understand the influence of alloying on the composition phase diagram of the kesterite material system and on the equilibrium relationship between Se(S) vapour pressure and temperature for the formation reactions of related metal chalcogenides. Second, the element diffusion and atom–lattice structure transformation at the interface between different phases during the CZTSSe crystallization process deserve more detailed study from the perspectives of theoretical calculations and experiments to help us better understand the atomic scale process of kesterite material synthesis and phase evolution.

We also further outlook the continued advancement of kesterite solar cells from several perspectives. First, meticulous optimization of the optical properties of the buffer and window layers is crucial.
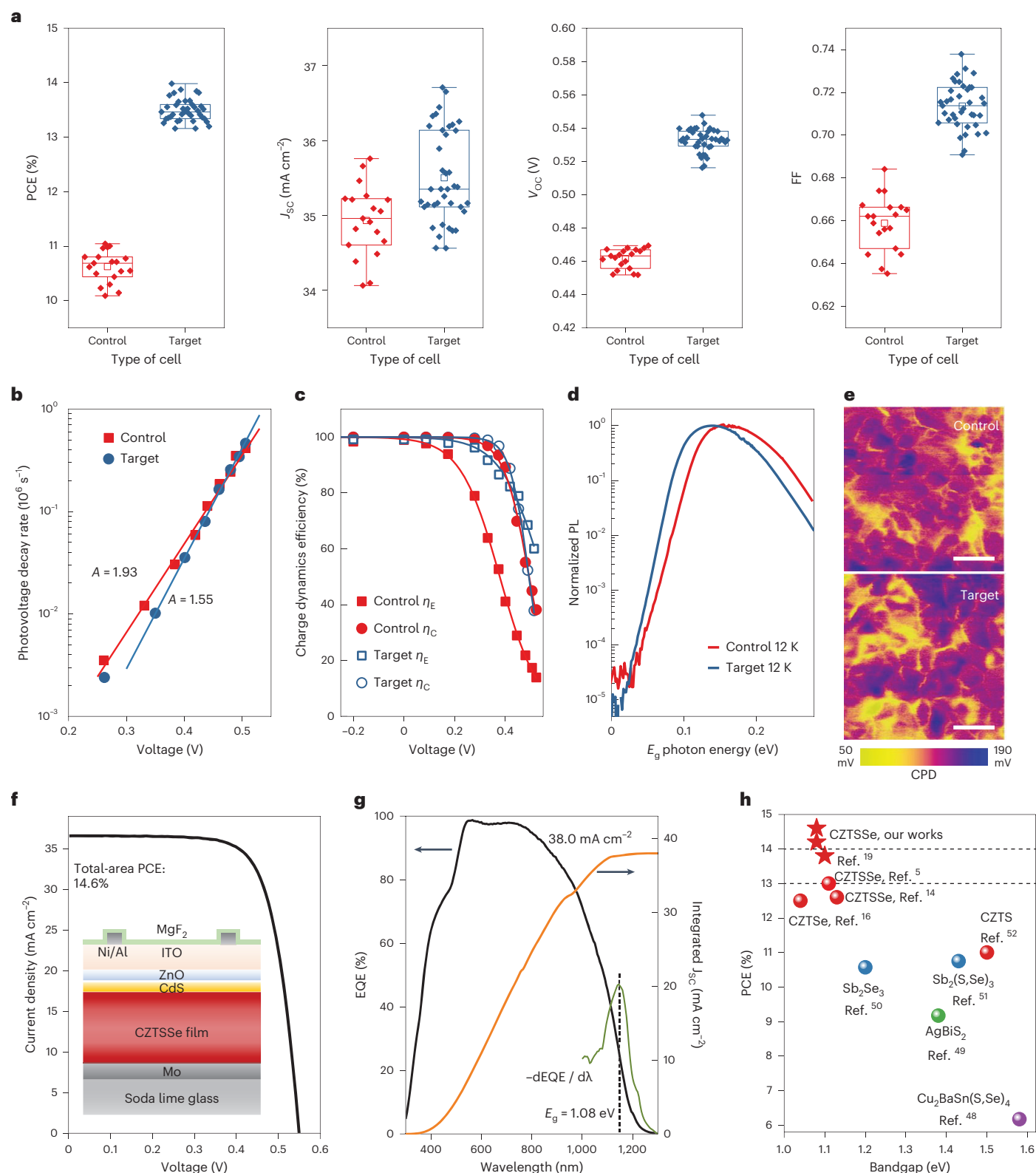
Fig. 4 | Solar cell characterization. a, Statistics of the cell performance parameters (centre line, median, box limits, upper and lower quartiles and raw data points are displayed in the box chart). Nineteen control cells and 39 target cells were included in the statistics. **b**, Voltage-dependent photovoltage decay rate of the cells. The solid lines depict the exponential fitting for determining the ideality factor (*A*) as described in Supplementary Note 1. **c**, Charge extraction (η_E) and collection (η_C) efficiencies of the cells with or without the elemental alloying. The solid lines are fitting curves as described in Supplementary Note 1.

d, PL spectra of the CZTSSe films measured at 12 K. **e**, Surface CPD images of the CZTSSe films. Scale bars, 2 μm. **f**, Current–voltage characteristics of the champion cell which has a total-area PCE of 14.6%. Inset: cell configuration. **g**, EQE spectrum and its integrated current density of the cell. The position of the absolute maxima of the differential EQE spectrum is used to estimate the bandgap of the CZTSSe absorber, which is marked up with the vertical dashed line. **h**, Champion performance of different emerging inorganic thin-film solar cells[5,14,16,19,48,54–57]. The dashed lines are guidance for the eyes.

Table 1 | Cell performance parameters of our and previously reported record cells

Device		Area (cm²)	PCE (%)	J_{sc} (mAcm⁻²)	V_{oc} (V)	FF	E_g (eV)	$E_g/q-V_{oc}$ (V)	J_{sc}/J_{sc}^{SQ}	$V_{oc}FF/V_{oc}^{SQ}FF^{SQ}$
This work	Control	0.28	11.3	35.9	0.460	0.684	1.06	0.600	0.80	0.44
	Target	0.28	14.6	36.6	0.550	0.724	1.08	0.530	0.82	0.55
	Certified	0.28	14.2	36.8	0.549	0.704		0.531	0.83	0.53
NJUPT cell[5]		0.11	13.0	33.6	0.529	0.729	1.11	0.581	0.76	0.51
IBM cell[14]		0.42	12.6	35.2	0.513	0.698	1.13	0.617	0.81	0.46
DGIST cell[15]		0.48	12.6	35.4	0.541	0.659	1.13	0.589	0.82	0.46
IOPCAS cell[19]		0.27	13.8	36.3	0.546	0.693	1.10	0.551	0.82	0.50

NJUPT, Nanjing University of Posts and Telecommunications; IBM, IBM (International Business Machines Corporation) T. J. Watson Research Center; DGIST, Daegu Gyeongbuk Institute of Science & Technology; IOPCAS, Institute of Physics Chinese Academy of Sciences.

This involves reducing layer thickness and employing wide-bandgap buffer materials, which can enhance the J_{sc}/J_{sc}^{SQ} values, making them comparable to those achieved by the leading Cu(In, Ga)Se₂ solar cells ($J_{sc}/J_{sc}^{SQ} \approx 0.88$). Simultaneously, increasing the effective thickness of kesterite absorbers and refining their crystallization process to eliminate fine grains and voids within the absorber layer are imperative, especially considering the non-reflective feature of the back-interface MoSe$_x$. Second, a more thorough comprehension of mass transport, ion exchange and structure evolution processes is necessary to gain better control over the growth of kesterite absorbers and address the aforementioned morphology issues. Improved regulation of alkali metal-assisted crystallization and environmental element equilibrium can also significantly contribute to this objective. Last, after addressing the morphology and deep defect issues of CZTSSe absorbers, a longer-term effort involves the introduction of a back field in the cell through gradient bandgap or heavy doping.

Conclusions
In summary, our study aimed to achieve significant advancements in kesterite solar cells by more precisely identifying and regulating deep defects in CZTSSe absorbers. Through device simulation and data correlation analysis, we made a step forward in experimentally identifying the primary deep defect responsible for charge loss in kesterite solar cells, which exhibits donor characteristics and is suggested to be Sn$_{Zn}$ antisite. Beyond the thermodynamic theoretical predictions, we proposed that the slow and incomplete Sn/Zn cation exchange in the multi-step reactions involved in CZTSSe crystallization is the kinetic mechanism for this defect formation. As guided by theoretical search, Ag, Ge and Cd have been introduced to synergistically regulate the CZTSSe fabrication, aimed at weakening the metal–chalcogen bond strength and the stability of intermediate phases to facilitate the cation exchange in the crystallization process. This multinary alloying strategy has obviously enhanced the reaction activity of Zn elements and thus facilitated the formation of ordered CZTSSe phases. Consequently, we significantly reduced the defect-induced charge loss in the CZTSSe absorber and achieved a remarkable high PCE of 14.6% (certified at 14.2%) in kesterite solar cells. Overall, this work has established a correlation between the defect formation and the microscopic crystallization process of CZTSSe from the perspective of cation-exchange kinetics and has explored a multinary alloying approach to regulate the defect formation. These understandings and the data-driven analysis method presented here also bring more avenues to identify and regulate defects in photovoltaic materials.

Methods
Materials
CuCl (99.999%, Alfa), Zn(CH₃COO)₂ (99.99%, Aladdin), SnCl₄ (99.998%, Macklin), AgCl (99.5%, Innochem), CdCl₂ (99.99%, Aladdin), GeO₂ (99.99%, Aladdin), 2-methoxyethanol (99.8%, Aladdin), thiourea (99.99%, Aladdin), Se pellets (99.999%, Zhong Nuo Advanced Material), CdSO₄·8/3H₂O (99.99%, Aladdin), ammonium chloride (≥99.5%, Sinopharm Chemical Reagent Co. Ltd.) and ammonium hydroxide (25.0–28.0%, Sinopharm Chemical Reagent Co. Ltd.) were used in this work. These chemicals except thiourea were used directly without further purification.

Precursor solution preparation
First, CuCl, Zn(CH₃COO)₂, SnCl₄ and thiourea were dissolved in 2-methoxyethanol and stirred at 60 °C to obtain a colourless solution. AgCl and CdCl₂ were then dissolved in the solution and stirred to get a final colourless solution. The concentrations of metal elements and thiourea are 1.88 M and 3.20 M, respectively. The molar ratio of I (Ag + Cu)/(II + IV) (Zn + Cd + Sn + Ge), II (Zn + Cd)/IV (Sn + Ge) and thiourea/metal are 0.75, 1.12 and 1.7, respectively. The Ge solution was prepared by dissolving GeO₂ in an ethylene glycol/ammonia solution mixed solvent (2:1). The alloying concentrations in these precursor solutions have been sequentially optimized by the order of Ag, Ge and Cd. In the optimization process, the above-mentioned molar ratio is kept unchanged.

Device fabrication
For the control cell fabrication, the CZTS precursor films were prepared by spin coating the precursor solution without the alloying elements on the cleaned Mo substrate at 3,000 r.p.m. s⁻¹ for 25 s, followed by annealing on a 280 °C hot plate in the air. The coating and annealing processes were repeated several times to obtain a precursor film with thickness of about 2 μm. The as-prepared precursor film was placed in a selenium-contained graphite box and selenized in a rapid thermal processing tube furnace with 80 sccm N₂ flow protection (1 atm). The annealing process is schematically shown in Supplementary Fig. 9. For the target cell, the GeO₂ solution was first spin coated on the Mo substrate at 4,200 r.p.m. for 40 s and then annealed on a hot plate at 300 °C for 10 s to form a thin layer as the Ge source for the alloying. Afterwards, the CZTS precursor solution with the alloying elements was used for the precursor film deposition. The film adopted the same selenization process to the control one. After selenization, a CdS buffer layer with a thickness of about 50 nm was deposited on top of the CZTSSe film by chemical bath deposition method. Window layers including ZnO and Sn:In₂O₃ (ITO) were deposited by radio frequency sputtering. Front grid electrode comprised of Ni and Al was deposited by thermal evaporation. Finally, a MgF₂ antireflection layer was thermally evaporated onto the cell to complete the fabrication process. The cells were separated from each other by mechanical scribing, and the design area of an individual cell is 0.28 cm² (4 × 7 mm²).

Material and device characterization
XRD patterns were collected using an X-ray diffractometer with Cu Ka as the radiation source (PANaltcal). Raman spectra measurements

were carried out on Raman spectrometer (Lab-RAM HR Evolution, HORIBA) using 532 nm and 325 nm lasers as the excitation source. SEM images were measured on Hitachi S4800. X-ray photoelectron spectroscopy measurement was carried out on an ESCALAB 250Xi (Thermo Fisher) instrument, and argon ion etching was used to obtain different depth measurements. The microstructure of the intermediate films was measured by a JEOL-F200CF STEM equipped with electron energy loss spectroscopy system. The sample for the STEM was prepared by a precision ion polishing system. Temperature-dependent steady-state and transient PL spectra were obtained on a PL spectrometer, FLS 900, Edinburgh Instruments, excited with a picosecond-pulsed diode laser at about 640 nm and cooling with a liquid helium system. The E_a^{PL} was fitted from the temperature-dependent PL intensity using equation $I_{PL}(T) = I_{PL}^0/(1 + A\exp(-E_a^{PL}/K_B T))$, where I_{PL}^0 is the initial PL intensity at low temperatures, A is a pre-factor, K_B is the Boltzmann constant and T is the temperature. KPFM images were obtained from Multimode 9, Bruker.

The current–voltage characteristics of the cells were recorded by a Keithley 2601 Source Meter under simulated AM 1.5G sunlight (100 mW cm^{-2}) calibrated with a Si reference cell (calibrated by the National Institute of Metrology of China). The voltage is scanned from −50 to 600 mV and the scanning rate is about 90 mV s^{-1}. Certification of the cell was performed in the National PV Industry Measurement and Testing Center and the certified aperture area of the cell was 0.2770 cm^2. All the measurements were performed in ambient conditions (air, 25 °C, uncontrolled humidity) and no preconditioning was applied before the measurements. EQE was measured by Enlitech QE-R system with calibrated Si and Ge diodes as references. Thermal admittance spectra were recorded by an electrochemical workstation (Versa STAT3, Princeton) in dark, and the cell temperature was controlled by a low-temperature probe station (Lakeshore TTPX). Modulated electrical transient measurements were carried out by our lab-made set-up (Supplementary Fig. 27) in which the cell was excited by a nanosecond laser at 640 nm and the transient signals were recorded by a sub-nanosecond-resolved digital oscilloscope with a sampling resistance of 50 Ω or 1 MΩ.

Device simulation
The device simulation of the CZTSSe solar cell was based on the wxAMPS programme derived from AMPS-1D[49,50]. The material parameters used in this simulation are listed in Supplementary Table 1. Notably, only the defect in the CZTSSe absorber was considered because the photoinduced electrons in other layers can be considered as majority carriers and the carrier recombination is negligible. In the CZTSSe, only discrete deep defect was considered because we found that the defect distribution shape has little influence on the cell performance provided the defect density and energy level are fixed. For the cell without sufficient back-surface field, an Ohmic contact between the CZTSSe and the Mo back electrode was considered with majority hole transfer rate (S_p) of 10^7 cm s^{-1}. The same electron transfer rate (S_n) was used for the front electrode/ITO interface. A surface reflectivity of 5% was used in the simulation.

To study voltage loss mechanism of the cell, an additional layer (E_g, 2.5 eV; affinity, 3 eV) with high hole concentration of 10^{18} cm^{-3} was introduced to provide back-surface field. The upper-limit V_{OC} of the cell was obtained by considering the back-surface field and using low defect concentration (10^{12} cm^{-3}) of CZTSSe absorber. The performance of cells with different defect concentration and σ has been simulated. In addition, for each defect condition, the cell with or without the back-surface field has also been considered. Under fixed defect condition, the voltage loss caused by the back-surface field was obtained by comparing the V_{OC} of the cells with and without the back-surface field. For calculating the voltage loss caused by the deep defect, the back-surface field was always considered, and the defect-induced voltage loss was calculated as the difference between the V_{OC} of the cell with certain defect properties to the upper-limit value. These simulations

found that when the cell efficiency is lower than 16%, the voltage loss is mainly caused by deep defect. As such, in the $J_{SC}/(V_{OC} \times FF)$-PCE relationship studies, back-surface field has not been considered.

DFT calculations
All calculations were carried out under the scheme of spin-polarized DFT using Cambridge Sequential Total Energy Package (CASTEP)[51]. The Perdew–Burke–Ernzerhof exchange-correlation functional within the generalized gradient approximation was employed to describe the exchange-correlation energy[52]. Semi-empirical corrected DFT (DFT-D) was introduced to guarantee a better description of the long-range electron interaction. Geometric optimization was performed for each lattice structure calculated in this study. Specifically, convergence tolerances were set as follows: maximum force of 0.03 eV Å^{-1}, maximum geometric energy change of 10^{-5} eV per atom, maximum displacement of 10^{-3} Å and maximum stress of 0.05 GPa. The plane wave energy cut-off was set at 600 eV, and the sampling in the Brillouin zone was set with $3 \times 3 \times 1$ by the Monkhorst–Pack method. In the calculations, supercells consisting of $Cu_{16}Sn_8Se_{24}$, Zn_8Se_8, $Cu_{15}AgSn_8Se_{24}$, $Cu_{16}Sn_7GeSe_{24}$ or Zn_7CdSe_8 were used. The configurations of these unalloyed and alloyed supercells are shown in Supplementary Figs. 6–8.

The change in the metal–Se bond energy was calculated by comparing the energy needed for removing a Se atom from the unalloyed and the alloyed CTSe (ZnSe) lattice (that is, forming a Se vacancy). The required energy was obtained by calculating the difference in total energy between the end-state and initial-state of the following reactions: Cu_2SnSe_3-Ag (or Ge) → Cu_2SnSe_3-Ag (or Ge) (V_{Se}) + Se, ZnSe-Cd → ZnSe-Cd (V_{Se}) + Se. Removing a Se atom requires the breaking of four metal–Se bonds. Specifically, in ZnSe-Cd, three Zn–Se bonds and one Cd–Se bond were involved, and in Cu_2SnSe_3-Ag (or Ge), three Cu(Sn)–Se bonds and one Ag(Ge)–Se bond were involved in the calculation. In this calculation, the Vanderbilt ultrasoft pseudopotential was used with a cut-off energy of 500 eV, and the maximum electron energy change is set at 10^{-6} eV per atom. The influence of Se chemical potential has not been considered here because in experiment the unalloyed and alloyed samples were reacted under the same selenium condition.

The free energies were calculated to evaluate the stability of the alloyed systems. The lattice configurations labelled as Cu_2SnSe_3, ZnSe, Cu_2SnSe_3-Ag (Se-CuAgSn$_2$), Cu_2SnSe_3-Ge (Se-Cu_2SnGe) and ZnSe-Cd in Supplementary Figs. 6–8 were considered in this calculation. For this computation, the Norm-conserving pseudopotential was used with a cut-off energy of 600 eV. The linear response density functional perturbation theory[53] implemented in the CASTEP code was used to obtain the free energies, enthalpies, entropies and zero-point energy in the quasi-harmonic approximation.

Reporting summary
Further information on research design is available in the Nature Portfolio Reporting Summary linked to this article.

Data availability
The data supporting the findings of this study are available within the main text, Supplementary Information and source data files. The structures used in the theoretical modelling are provided as Supplementary Datasets. Source data are provided with this paper.

References
1. Polman, A., Knight, M., Garnett, E. C., Ehrler, B. & Sinke, W. C. Photovoltaic materials: present efficiencies and future challenges. *Science* **352**, aad4424 (2016).
2. Park, J. S., Kim, S., Xie, Z. & Walsh, A. Point defect engineering in thin-film solar cells. *Nat. Rev. Mater.* **3**, 194–210 (2018).
3. Mitzi, D. B., Gunawan, O., Todorov, T. K., Wang, K. & Guha, S. The path towards a high-performance solution-processed kesterite solar cell. *Sol. Energy Mater. Sol. Cells* **95**, 1421–1436 (2011).

4. Siebentritt, S. & Schorr, S. Kesterites—a challenging material for solar cells. *Prog. Photovoltaics Res. Appl.* **20**, 512–519 (2012).

5. Gong, Y. et al. Elemental de-mixing-induced epitaxial kesterite/CdS interface enabling 13%-efficiency kesterite solar cells. *Nat. Energy* **7**, 966–977 (2022).

6. Antunez, P. D., Bishop, D. M., Luo, Y. & Haight, R. Efficient kesterite solar cells with high open-circuit voltage for applications in powering distributed devices. *Nat. Energy* **2**, 884–890 (2017).

7. Li, J. et al. Unveiling microscopic carrier loss mechanisms in 12% efficient $Cu_2ZnSnSe_4$ solar cells. *Nat. Energy* **7**, 754–764 (2022).

8. Chen, S., Walsh, A., Gong, X.-G. & Wei, S.-H. Classification of lattice defects in the kesterite Cu_2ZnSnS_4 and $Cu_2ZnSnSe_4$ Earth-abundant solar cell absorbers. *Adv. Mater.* **25**, 1522–1539 (2013).

9. Kim, S., Márquez, J. A., Unold, T. & Walsh, A. Upper limit to the photovoltaic efficiency of imperfect crystals from first principles. *Energy Environ. Sci.* **13**, 1481–1491 (2020).

10. Larramona, G. et al. Fine-tuning the Sn content in CZTSSe thin films to achieve 10.8% solar cell efficiency from spray-deposited water–ethanol-based colloidal inks. *Adv. Energy Mater.* **5**, 1501404 (2015).

11. Yuan, Z. et al. Engineering solar cell absorbers by exploring the band alignment and defect disparity: the case of Cu- and Ag-based kesterite compounds. *Adv. Funct. Mater.* **25**, 6733–6743 (2015).

12. Gong, Y. et al. Ag incorporation with controlled grain growth enables 12.5% efficient kesterite solar cell with open circuit voltage reached 64.2% Shockley–Queisser limit. *Adv. Funct. Mater.* **31**, 2101927 (2021).

13. Du, Y. et al. Defect engineering in Earth-abundant $Cu_2ZnSn(S,Se)_4$ photovoltaic materials via Ga^{3+}-doping for over 12% efficient solar cells. *Adv. Funct. Mater.* **31**, 2010325 (2021).

14. Wang, W. et al. Device characteristics of CZTSSe thin-film solar cells with 12.6% efficiency. *Adv. Energy Mater.* **4**, 1301465 (2014).

15. Son, D.-H. et al. Effect of solid-H_2S gas reactions on CZTSSe thin film growth and photovoltaic properties of a 12.62% efficiency device. *J. Mater. Chem. A* **7**, 25279–25289 (2019).

16. Li, J. et al. Defect control for 12.5% efficiency $Cu_2ZnSnSe_4$ kesterite thin-film solar cells by engineering of local chemical environment. *Adv. Mater.* **32**, 2005268 (2020).

17. Su, Z. et al. Device postannealing enabling over 12% efficient solution-processed Cu_2ZnSnS_4 solar cells with Cd^{2+} substitution. *Adv. Mater.* **32**, 2000121 (2020).

18. Guo, H. et al. Band-gap-graded $Cu_2ZnSn(S,Se)_4$ drives highly efficient solar cells. *Energy Environ. Sci.* **15**, 693–704 (2022).

19. Zhou, J. et al. Control of the phase evolution of kesterite by tuning of the selenium partial pressure for solar cells with 13.8% certified efficiency. *Nat. Energy* **8**, 526–535 (2023).

20. Bourdais, S. et al. Is the Cu/Zn disorder the main culprit for the voltage deficit in kesterite solar cells? *Adv. Energy Mater.* **6**, 1502276 (2016).

21. Duan, B. et al. Underlying mechanism of the efficiency loss in CZTSSe solar cells: disorder and deep defects. *Sci. China Mater.* **63**, 2371–2396 (2020).

22. He, M. et al. Kesterite solar cells: insights into current strategies and challenges. *Adv. Sci.* **8**, 2004313 (2021).

23. Yoo, H. et al. Investigation of the solid state reactions by time-resolved X-ray diffraction while crystallizing kesterite $Cu_2ZnSnSe_4$ thin films. *Thin Solid Films* **535**, 73–77 (2013).

24. Gunawan, O., Todorov, T. K. & Mitzi, D. B. Loss mechanisms in hydrazine-processed $Cu_2ZnSn(Se,S)_4$ solar cells. *Appl. Phys. Lett.* **97**, 233506 (2010).

25. Kumar, A. & Thakur, A. D. Comprehensive loss modeling in Cu_2ZnSnS_4 solar cells. *Curr. Appl. Phys.* **19**, 1111–1119 (2019).

26. Xu, X. et al. Efficient and composition-tolerant kesterite $Cu_2ZnSn(S, Se)_4$ solar cells derived from an in situ formed multifunctional carbon framework. *Adv. Energy Mater.* **11**, 2102298 (2021).

27. Zhou, J. et al. Regulating crystal growth via organic lithium salt additive for efficient kesterite solar cells. *Nano Energy* **89**, 106405 (2021).

28. Levcenko, S. et al. Deep defects in $Cu_2ZnSn(S,Se)_4$ solar cells with varying Se content. *Phys. Rev. Appl.* **5**, 024004 (2016).

29. Kim, S., Park, J. S. & Walsh, A. Identification of killer defects in kesterite thin-film solar cells. *ACS Energy Lett.* **3**, 496–500 (2018).

30. Xu, Y., Yang, J., Chen, S. & Gong, X. G. Defect-assisted nonradiative recombination in $Cu_2ZnSnSe_4$: a comparative study with Cu_2ZnSnS_4. *Phys. Rev. Mater.* **5**, 025403 (2021).

31. Yin, X., Tang, C., Sun, L., Shen, Z. & Gong, H. Study on phase formation mechanism of non- and near-stoichiometric $Cu_2ZnSn(S,Se)_4$ film prepared by selenization of Cu–Sn–Zn–S precursors. *Chem. Mater.* **26**, 2005–2014 (2014).

32. Hages, C. J., Koeper, M. J., Miskin, C. K., Brew, K. W. & Agrawal, R. Controlled grain growth for high performance nanoparticle-based kesterite solar cells. *Chem. Mater.* **28**, 7703–7714 (2016).

33. Giraldo, S. et al. How small amounts of Ge modify the formation pathways and crystallization of kesterites. *Energy Environ. Sci.* **11**, 582–593 (2018).

34. Hsu, W. C., Bob, B., Yang, W., Chung, C. H. & Yang, Y. Reaction pathways for the formation of $Cu_2ZnSn(Se,S)_4$ absorber materials from liquid-phase hydrazine-based precursor inks. *Energy Environ. Sci.* **5**, 8564–8571 (2012).

35. Goodenough, J. B. Electronic and ionic transport properties and other physical aspects of perovskites. *Rep. Prog. Phys.* **67**, 1915–1993 (2004).

36. Cheng, Y. Q. & Ma, E. Atomic-level structure and structure–property relationship in metallic glasses. *Prog. Mater. Sci.* **56**, 379–473 (2011).

37. Liu, M. & Meng, S. *Atomly Modernize the Materials Science* (Chinese Academy of Sciences, 2020); https://atomly.net/#/matdata

38. Liu, M. & Meng, S. Atomly.net materials database and its application in inorganic chemistry. *Sci. Sin. Chim.* **53**, 19–25 (2023).

39. Hasaneen, M. F., Ali, H. M., Abd El-Raheem, M. M. & Abdel Hakeem, A. M. Structure and optical properties of thermally evaporated Te doped ZnSe thin films. *Mater. Sci. Eng. B* **262**, 114704 (2020).

40. Paier, J., Asahi, R., Nagoya, A. & Kresse, G. Cu_2ZnSnS_4 as a potential photovoltaic material: a hybrid Hartree-Fock density functional theory study. *Phys. Rev. B* **79**, 115126 (2009).

41. Yee, Y. S., Magyari-Köpe, B., Nishi, Y., Bent, S. F. & Clemens, B. M. Deep recombination centers in $Cu_2ZnSnSe_4$ revealed by screened-exchange hybrid density functional theory. *Phys. Rev. B* **92**, 195201 (2015).

42. Walter, T., Herberholz, R., Müller, C. & Schock, H. W. Determination of defect distributions from admittance measurements and application to $Cu(In,Ga)Se_2$ based heterojunctions. *J. Appl. Phys.* **80**, 4411–4420 (1996).

43. Shi, J., Li, D., Luo, Y., Wu, H. & Meng, Q. Opto-electro-modulated transient photovoltage and photocurrent system for investigation of charge transport and recombination in solar cells. *Rev. Sci. Instrum.* **87**, 123107 (2016).

44. Li, Y. et al. Exploiting electrical transients to quantify charge loss in solar cells. *Joule* **4**, 472–489 (2020).

45. Luckert, F. et al. Optical properties of high quality $Cu_2ZnSnSe_4$ thin films. *Appl. Phys. Lett.* **99**, 062104 (2011).

46. Tennyson, E. M. et al. Nanoimaging of open-circuit voltage in photovoltaic devices. *Adv. Energy Mater.* **5**, 1501142 (2015).

47. Kang, Z. et al. Kelvin probe force microscopy for perovskite solar cells. *Sci. Chin. Mater.* **62**, 776–789 (2019).

48. Teymur, B. et al. Top stack optimization for $Cu_2BaSn(S, Se)_4$ photovoltaic cell leads to improved device power conversion efficiency beyond 6%. *Adv. Energy Mater.* **12**, 2201602 (2022).

49. Zhu, H., Kalkan, A. K., Hou, J. Y. & Fonash, S. J. Applications of AMPS-1D for solar cell simulation. *AIP Conf. Proc.* **462**, 309–314 (1999).

50. Liu, Y., Sun, Y. & Rockett, A. A new simulation software of solar cells—WxAMPS. *Sol. Energy Mater. Sol. Cells* **98**, 124–128 (2012).

51. Clark, S. J. et al. First principles methods using CASTEP. *Z. Kristallogr.* **220**, 567–570 (2005).

52. Perdew, J. P., Burke, K. & Ernzerhof, M. Generalized gradient approximation made simple. *Phys. Rev. Lett.* **77**, 3865–3868 (1996).

53. Baroni, S., de Gironcoli, S., Corso, A. D. & Giannozzi, P. Phonons and related crystal properties from density-functional perturbation theory. *Rev. Mod. Phys.* **73**, 515–562 (2001).

54. Wang, Y. et al. Cation disorder engineering yields $AgBiS_2$ nanocrystals with enhanced optical absorption for efficient ultrathin solar cells. *Nat. Photon.* **16**, 235–241 (2022).

55. Zhao, Y. et al. Regulating deposition kinetics via a novel additive-assisted chemical bath deposition technology enables fabrication of 10.57%-efficiency Sb_2Se_3 solar cells. *Energy Environ. Sci.* **15**, 5118–5128 (2022).

56. Chen, X. et al. Solvent-assisted hydrothermal deposition approach for highly-efficient $Sb_2(S,Se)_3$ thin-film solar cells. *Adv. Energy Mater.* **13**, 2300391 (2023).

57. Yan, C. et al. Cu_2ZnSnS_4 solar cells with over 10% power conversion efficiency enabled by heterojunction heat treatment. *Nat. Energy* **3**, 764–772 (2018).

Acknowledgements

Author contributions

J.S., J.W. and Q.M. conceived the idea. J.S. did the device simulation, data analysis, device characterization and theoretical calculations and proposed the kinetic mechanism. J.W. and J.Z. fabricated solar cells and did the material/device characterization. F.M. did the STEM characterization and data analysis. X.X., K.Y. and L.L. participated in the device fabrication, optimization and data collection. M.J. and B.Z. participated in the device fabrication. H.W., Y.L. and D.L. participated in the experiment design and discussions. J.S. and Q.M. participated in paper writing and revising. All authors were involved in the discussions and approved the paper.

Competing interests

The authors declare no competing interests.

Additional information

Supplementary information The online version contains supplementary material available at https://doi.org/10.1038/s41560-024-01551-5.

Correspondence and requests for materials should be addressed to Qingbo Meng.

Peer review information *Nature Energy* thanks Jonathan Staaf Scragg and the other, anonymous, reviewer(s) for their contribution to the peer review of this work.

Reprints and permissions information is available at www.nature.com/reprints.